Range-Dependence Compensation in STAP for Arbitrary Engagement Geometries and Receiver Antenna Arrays

Philippe Ries[1], Sébastien de Grève[1], Xavier Neyt[2], Fabian D. Lapierre[2] , and Jacques G. Verly[1]

[1] Department of Electrical Engineering and Computer Science, University of Liège,
Grande Traverse, 10
B-4000 Liège
BELGIUM

[2] Department of Electrical Engineering, Royal Military Academy,
Avenue de la Renaissance, 30
B-1000 Brussels
BELGIUM

{ries;degreve}@montefiore.ulg.ac.be, jacques.verly@ulg.ac.be, xne@rma.ac.be, f_lapierre@fastmail.fm,

ABSTRACT

Space-time adaptive processing (STAP) is a well-suited technique to detect slow-moving targets in the presence of a strong interference background. The secondary-data snapshots used to estimate the optimum weight vector are range-dependent (RD) when the operating conditions differ from those of a radar using a uniform linear array (ULA) in a monostatic sidelooking configuration. This prevents the STAP processor from achieving its optimum performance. We first give an overview of signal processing methods that were proposed early on to tackle the RD problem, such as Doppler warping, angle-Doppler compensation, adaptive angle-Doppler compensation, and derivative-based updating. These methods mitigate the range-dependence only for highly-directive antennas or operating scenarios giving rise to only moderate range-dependence of the secondary data. We then present a registration-based compensation (RBC) method developed in our research group that can handle the range-dependence for bistatic radars using a ULA with omnidirectional sensors and an arbitrary crab angle. Finally, we propose an extension of the RBC method that allows one to handle, not only arbitrary engagement geometries, but also arbitrary antennas, and thus conformal antenna arrays.

1.0 INTRODUCTION

The problem addressed is the detection by an airborne radar of slow-moving targets in the presence of strong interference in the signal received. Besides possible target echoes, the received signal also contains a (thermal) noise part and an interference part, the latter being typically due to clutter returns and possible jamming signals. The most important interference signal is the clutter return due to the ground. Hence, the detection of a target requires one to be able to discriminate between target signals and clutter returns. All signals received can be characterized in terms of range by the time delay between the transmission of the signal and the reception of the echoes and in terms of relative radial velocity by the Doppler frequency. Range and radial velocity can be measured by a pulse-Doppler radar [1] using a train of M pulses. The

Ries, P.; de Grève, S.; Neyt, Z.; Lapierre, F.D.; Verly, J.G. (2006) Range-Dependence Compensation in STAP for Arbitrary Engagement Geometries and Receiver Antenna Arrays. In *Bistatic-Multistatic Radar and Sonar Systems* (pp. 28-1 – 28-26). Meeting Proceedings RTO-MP-SET-095, Paper 28. Neuilly-sur-Seine, France: RTO. Available from: http://www.rto.nato.int/abstracts.asp.

Doppler-induced pulse-to-pulse phase shift in the echoes received at a given range allows one to distinguish between fast-moving targets and ground clutter. Indeed, fast-moving targets will present a Doppler shift larger than the Doppler spread of the clutter. However, slow-moving targets will typically remain hidden in the clutter spectrum.

This is where space-time adaptive processing (STAP) comes into play [2]. An N-element antenna array, typically a uniform linear array (ULA), mounted on the receiver platform offers an additional way of characterizing the received signals, namely in terms of their angles of arrival. This is achieved by exploiting the angle-of-arrival-dependent element-to-element phase shift. The received signals can thus be discriminated both in space (the angle of arrival) and in time (the Doppler frequency). This is the idea underlying STAP. In the angle-Doppler space, the interference and, in particular, the clutter have a very specific signature allowing one to filter them out while preserving the slow-moving targets. Thus, STAP makes it possible to detect the slow-moving targets, which would remain hidden in the interference background in the case of a classical pulse-Doppler radar. In STAP, a radar return recorded at a given range for the M pulses and the N antenna elements is of size N x M and is called a snapshot.

Early radar systems based on STAP used a monostatic (MS) configuration, i.e. a configuration where the transmitter and the receiver are located on the same platform, as well as a ULA, generally in a sidelooking position. However, a bistatic (BS) configuration, i.e. a configuration where the transmitter and the receiver are located on two independently moving platforms, offers numerous advantages over an MS configuration. The most important are the following. (1) A BS radar system is likely to detect targets that use stealth technology, which is designed to reflect incoming electromagnetic energy into directions other than the direction of illumination [3]. Since the energy is conserved, the target signature is increased at some or all angles other than the angle of the incoming wave. (2) The receiver platform does not emit any electromagnetic radiation. The platform is thus immune to anti-radiation missiles [1] and the receiver is less likely to be jammed by the enemy [4]. (3) During military operations, the transmitter can be in a "safe" standoff position, far away from the theater of operations.

Unfortunately, these advantages come at the cost of increased complexity in the processing of the signals recorded by the BS system. For example, successful BS operation requires a precise synchronization between the transmitter and the receiver. However, in this paper, we focus on another problem, i.e. the fact that the clutter signature is much more complex in BS systems than in MS systems, even when assuming that the receiver uses sidelooking ULAs. Indeed, the rejection of the clutter return at a given range requires the computation of a space-time filter involving the estimation of the interference-plus-noise (I+N) covariance matrix corresponding to this range. This covariance matrix is typically estimated from the snapshots recorded at neighboring ranges; these snapshots constitute the so-called secondary data. For BS radars, the secondary-data snapshots are not identically distributed with respect to range. It is thus *not* acceptable to estimate the I+N covariance matrix by simply averaging the sample covariance matrices corresponding to the secondary-data snapshots. A STAP filter neglecting the range-dependent (RD) statistics of the secondary data leads to severe losses in detection performance. This problem is called the range-dependence (RD) problem. This paper focuses on range-dependence compensation (RDC) in BS radar systems.

We first give an overview of the various signal processing techniques proposed to tackle the RD problem. A common characteristic of most RDC methods is the attempt to register the clutter signatures at auxiliary ranges with the clutter signature at the range of interest. This is, for example, the case in Doppler warping (DW) [5], angle-Doppler compensation (ADC) [6], adaptive angle-Doppler compensation (A^2DC) [7], and high-order Doppler warping (HODW) [8], all of which, however, achieve only partial registration and, thus, work only for highly-directive antenna beampatterns. Another example of an RDC method is derivative-based updating (DBU) [9]. However, DBU achieves near optimum performance only for some BS configurations and requires a very large set of secondary data. We then present the registration-based compensation (RBC) method [10], which achieves near optimum RDC with a low sample support

requirement and a reasonable computational complexity. The RBC method is based on a thorough mathematical description of the locus of the clutter signature in the angle-Doppler space. This method can, for any antenna pattern, achieve complete registration of the clutter signatures of the secondary data with that at the range of interest. This feature leads to near-optimum performance. Finally, we describe how the RBC method of [10] can be generalized to BS systems using conformal antenna arrays (CAA) at the receiver instead of ULAs [11].

The paper is organized as follows. Section 2 reviews the standard notions of snapshot and optimum processor as well as the associated notations. Section 3 reviews the crucial concept of direction-Doppler (DD) curves and surfaces. Section 4 reviews the DW, ADC, A^2DC, and DBU methods. Section 5 discusses the more recent RBC method. Section 6 introduces a flight configuration parameter estimation algorithm. Section 7 extends the notion of DD curves to CAAs. In Section 8, the RBC method is extended to CAAs. Section 9 shows some preliminary results. Section 10 concludes.

2.0 SNAPSHOTS AND OPTIMUM PROCESSOR

2.1 Snapshots

In each coherent processing interval, a coherent train of M pulses is emitted from the transmitter T. The returns are sensed at each of the N elements of the antenna array at the receiver R. Finally, the sensed returns are sampled at a number of discrete ranges (also called range cells or range gates) covering the range interval of interest. Ranges are indexed with $k \in L = \{0,1,...,L-1\}$. We regard the data as a sequence of $M \times N$ 2D data arrays (snapshots) at successive ranges k. The $M \times N$ snapshot corresponding to a specific k and to a single scatterer S characterized by its normalized spatial frequency ν_s and its normalized Doppler frequency ν_d can be written as the $MN \times 1$ vector [12]

$$\underline{\mathbf{y}}(\nu_s,\nu_d) = \beta_r \, \underline{\mathbf{v}}(\nu_s,\nu_d) = \beta_r \left(\underline{\mathbf{b}}(\nu_d) \otimes \underline{\mathbf{a}}(\nu_s)\right), \qquad (1)$$

where β_r is found from the radar equation, $\underline{\mathbf{v}}(\nu_s,\nu_d)$ is the $MN \times 1$ steering vector, $\otimes$ is the Kronecker product, $\underline{\mathbf{a}}(\nu_s)$ is the $N \times 1$ spatial steering vector, and $\underline{\mathbf{b}}(\nu_d)$ is the $M \times 1$ temporal steering vector. For ULAs, we have [13]

$$\underline{\mathbf{a}}(\nu_s) = (1 ... e^{j2\pi\nu_s n} ... e^{j2\pi\nu_s (N-1)})^T \qquad (2)$$

$$\underline{\mathbf{b}}(\nu_d) = (1 ... e^{j2\pi\nu_d m} ... e^{j2\pi\nu_d (M-1)})^T. \qquad (3)$$

If we hypothesize that we are dealing with a single target with parameters (ν_s^t,ν_d^t) and interference consisting of clutter and noise (and no jammer), we can model the snapshot at each range k by

$$\underline{\mathbf{y}}_k = \underline{\mathbf{y}}_{t,k} + \underline{\mathbf{y}}_{c,k} + \underline{\mathbf{y}}_{n,k}.$$

The target snapshot $\underline{\mathbf{y}}_{t,k}$ is given by Eq. (1), where we use the appropriate target parameters (ν_s^t,ν_d^t). The clutter snapshot $\underline{\mathbf{y}}_{c,k}$ is found by integrating $\underline{\mathbf{y}}(\nu_s,\nu_d)$ over the 3D isorange (parameterized with the vector $\underline{\mathbf{r}}_i(\psi_i)$), i.e.

$$\underline{\mathbf{y}}_{c,k} = \int_0^{2\pi} \beta_c(\underline{\mathbf{r}}_i(\psi_i))\, \underline{\mathbf{v}}(\nu_s(\underline{\mathbf{r}}_i(\psi_i)), \nu_d(\underline{\mathbf{r}}_i(\psi_i)))\, d\psi_i, \qquad (4)$$

where $\beta_c(\underline{\mathbf{r}}_i(\psi_i))$ is the complex-valued random amplitude corresponding to the clutter patch designated by $\underline{\mathbf{r}}_i(\psi_i)$. We assume that $\underline{\mathbf{y}}_{c,k}$ is wide-sense stationary with respect to space and time. It is thus characterized by a constant covariance matrix

$$\underline{\underline{\mathbf{R}}}_{c,k} = E\{\underline{\mathbf{y}}_{c,k}\underline{\mathbf{y}}_{c,k}^{\dagger}\} = \int_0^{2\pi} \sigma_c(\underline{r}(\psi_i))\underline{v}(\underline{r}(\psi_i))\underline{v}^{+}(\underline{r}(\psi_i))d\psi_i$$

where $\sigma_c(\underline{r}(\psi_i)) = E\{|\beta_c(\underline{r}(\psi_i))|^2\}$ is a measure of the signal power scattered by the clutter patch at $\underline{r}(\psi_i)$. The noise snapshot $\underline{\mathbf{y}}_{n,k}$ is assumed to be spatially and temporally white and independent of range. Thus, we have $\underline{\underline{\mathbf{R}}}_{n,k} = E\{\underline{\mathbf{y}}_{n,k}\underline{\mathbf{y}}_{n,k}^{\dagger}\} = P_n \underline{\underline{\mathbf{I}}}$, where P_n is the noise power. The I+N snapshot $\underline{\mathbf{y}}_{q,k} = \underline{\mathbf{y}}_{c,k} + \underline{\mathbf{y}}_{n,k}$ is thus characterized by the I+N covariance matrix $\underline{\underline{\mathbf{R}}}_{q,k} = E\{\underline{\mathbf{y}}_{q,k}\underline{\mathbf{y}}_{q,k}^{\dagger}\}$.

1.1 Optimum processor (OP)

The optimum processor successively deals with all range gates l of interest. The corresponding range is denoted by R_l. For each l, the primary input to the STAP detector is the snapshot $\underline{\mathbf{y}}_l$. Secondary inputs are specific values of ν_s and ν_d and the theoretical $\underline{\underline{\mathbf{R}}}_{q,l}$ at l. The triplet (ν_s, ν_d, R_l) constitutes the "target hypothesis." The weight vector that maximizes the output SINR is given by [14]

$$\underline{\mathbf{w}}_o(\nu_s, \nu_d, R_l) = \alpha \underline{\underline{\mathbf{R}}}_{q,l}^{-1} \underline{\mathbf{v}}(\nu_s, \nu_d), \qquad (5)$$

where α is an arbitrary complex constant. The detection statistic is the complex scalar $z = \underline{\mathbf{w}}_o^{\dagger}(\nu_s, \nu_d, R_l)\underline{\mathbf{y}}_l$. Its magnitude is compared to a threshold λ to determine whether the target hypothesis is true or false. In practice, $\underline{\underline{\mathbf{R}}}_{q,l}$ is estimated from the snapshots via [12]

$$\hat{\underline{\underline{\mathbf{R}}}}_{q,l} = \frac{1}{N_l} \sum_{k \in S_l} \tilde{\underline{\underline{\mathbf{R}}}}_{q,k} \quad \text{with} \quad \tilde{\underline{\underline{\mathbf{R}}}}_{q,k} = \underline{\mathbf{y}}_{q,k}\underline{\mathbf{y}}_{q,k}^{\dagger}, \qquad (6)$$

where S_l is a set of indices of range gates used for estimation and assumed here to consist of N_l successive indices centered on l (with l excluded). $\hat{\underline{\underline{\mathbf{R}}}}_{q,l}$ is "maximum likelihood" only if the $\underline{\mathbf{y}}_{q,k}$'s are independent and identically distributed (iid) with respect to range and have complex Gaussian probability density functions [15]. Unfortunately, in virtually all configurations, the $\underline{\mathbf{y}}_{q,k}$'s are not iid with respect to range.

The performance of a processor using an arbitrary weight vector $\underline{\mathbf{w}}$ is measured by the signal-to-interference-plus-noise (SINR) loss given by [12]

$$\mathrm{SINR}_{\mathrm{L}} = \frac{\mathrm{SINR}}{\mathrm{SNR}_0} = \frac{P_n \left| \underline{\mathbf{w}}^{\dagger} \underline{\mathbf{v}} \right|^2}{(\underline{\mathbf{w}}^{\dagger} \underline{\underline{\mathbf{R}}}_{q,l} \underline{\mathbf{w}})(\underline{\mathbf{v}}^{\dagger} \underline{\mathbf{v}})}, \quad (7)$$

where SNR_o is the SINR in the absence of clutter. The SINR_L is an important measure of performance because the probability of detection is directly related to SINR_L [16]. Optimum performance, i.e. maximum SINR_L, is achieved for $\underline{\mathbf{w}} = \underline{\mathbf{w}}_o$.

3.0 DIRECTION-DOPPLER (DD) CURVES AND SURFACES

The three important physical parameters associated with each scatterer S are its BS range R_b, the angle of arrival ξ_S with respect to the ULA axis, and the relative velocity v_R, which is the sum of the relative radial velocities between T and S and between S and R. The related parameters that are more directly measured from the radar returns are the roundtrip delay τ_{rt}, the spatial frequency f_s, and the Doppler frequency f_d. For a stationary S, $\tau_{rt} = R_b/c$, $f_s = \cos\xi_s/\lambda_c$, and $f_d = v_R/\lambda_c$, where λ_c is the carrier wavelength and c is the speed of light [2].

All scatterers S characterized by the same R_b are located on an isorange surface, which is an ellipsoid of revolution with foci at T and R. The intersection of this surface with the ground is an isorange curve, which is an ellipse (parameterized with the polar angle ψ) in the case of flat (horizontal) ground, as is assumed here. For any given configuration and range, all stationary scatterers S at this range map onto a curve showing the relation between f_s and f_d for any such S. This curve is called clutter power spectrum (PS) locus, angle-Doppler curve, or direction-Doppler (DD) curve [11,12,17,18,19]. DD curves are typically represented in terms of the normalized spatial frequency $\nu_s = (\lambda/2) f_s$ and of the normalized Doppler frequency $\nu_d = f_d / PRF$, where PRF is the pulse repetition frequency. The equations of the BS DD curves are obtained by expressing ν_s and ν_d as functions of ψ, i.e. $\nu_s = g_1(\psi)$ and $\nu_d = g_2(\psi)$. The derivation of the $g_i(\psi)$'s is lengthy and, thus, not given here. The reader should consult [13] for details.

Figure 1 shows that BS DD curves vary significantly with configuration and range. The variation of these curves with range for any particular configuration is one of the most visible manifestations of the RD problem.

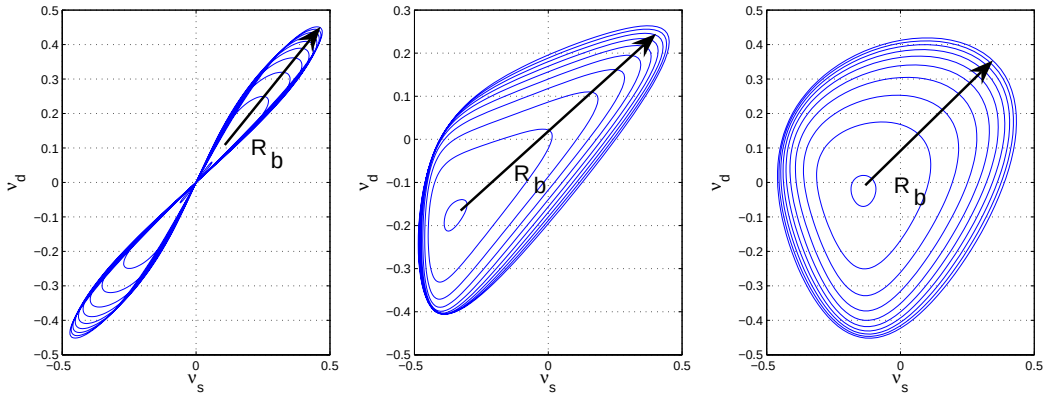

Figure 1. DD curves for different BS configurations and different BS ranges R_b.

Both in the MS case and in the BS case, DD curves depend only on the flight configuration parameters such as the relative positions of the platform(s), their height, their velocity vectors, and the crab angle of the receiver antenna. All these parameters are lumped into the flight configuration parameter vector $\underline{\theta}$.

Another concept giving valuable insight into the RD problem is that of DD surface. A DD surface is obtained by stacking the DD curves at increasing R_b on top of each other. This gives rise to a surface in the (ν_s, ν_d, R_b) space as shown in Fig. 2. The surface clearly deviates from that of a cylinder, and this indicates that the configuration is range-dependent.

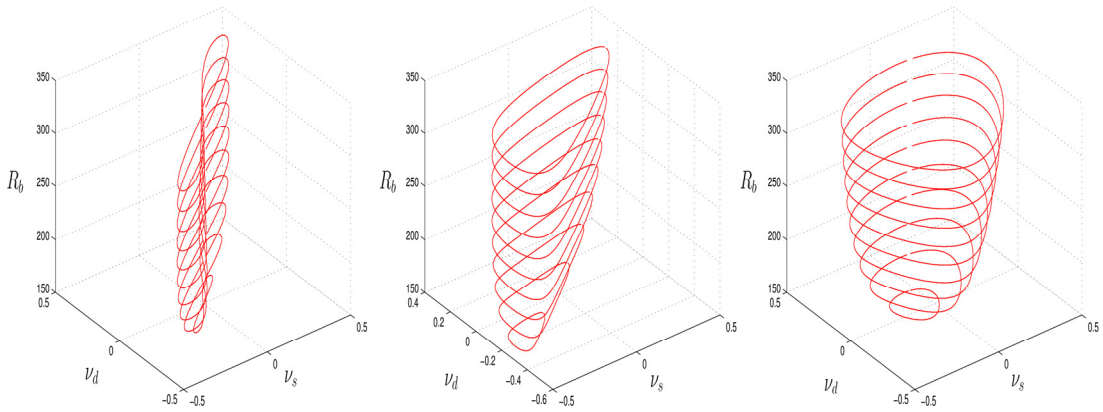

Figure 2. DD surfaces corresponding to the BS configurations of Fig. 1.

4.0 EXISTING METHODS OF RANGE-DEPENDENCE COMPENSATION (RDC)

In this section, we review the DW, ADC, A^{2}DC, and DBU methods. All but the DBU method can be explained in terms of registration of DD curves.

4.1 Doppler warping (DW)

The DW method was initially developed for nearly-sidelooking MS configurations [5]. DW registers the DD curves at only one specific (ν_s,ν_d) point. This is done at each range k by subtracting from ν_d in Eq. (1) a Doppler shift Δ_k such that the clutter ridge at range k is brought into registration with the clutter ridge at the range of interest, say l, at the selected value of ν_s. This transformation thus considers only a translation along the Doppler-frequency axis. This is illustrated in Fig. 3, where Figs. 3a and 3b show the DD curves at the different ranges before and after registration, respectively. Applying the Doppler shift Δ_k is equivalent to applying the matrix

$$\underline{\underline{\mathbf{T}}}_{kl}^{DW} = \text{diag}\{1\, e^{-j2\pi\Delta_k} \ldots e^{-j2\pi\Delta_k(M-1)}\} \otimes \underline{\underline{\mathbf{I}}}$$

to the snapshot $\underline{\mathbf{y}}_k$ at range k, yielding

$$\underline{\mathbf{y}}_{kl}^{DW} = \underline{\underline{\mathbf{T}}}_{kl}^{DW}\, \underline{\mathbf{y}}_k.$$

The sample matrix inversion (SMI) [14] algorithm can then be applied to the registered snapshots.

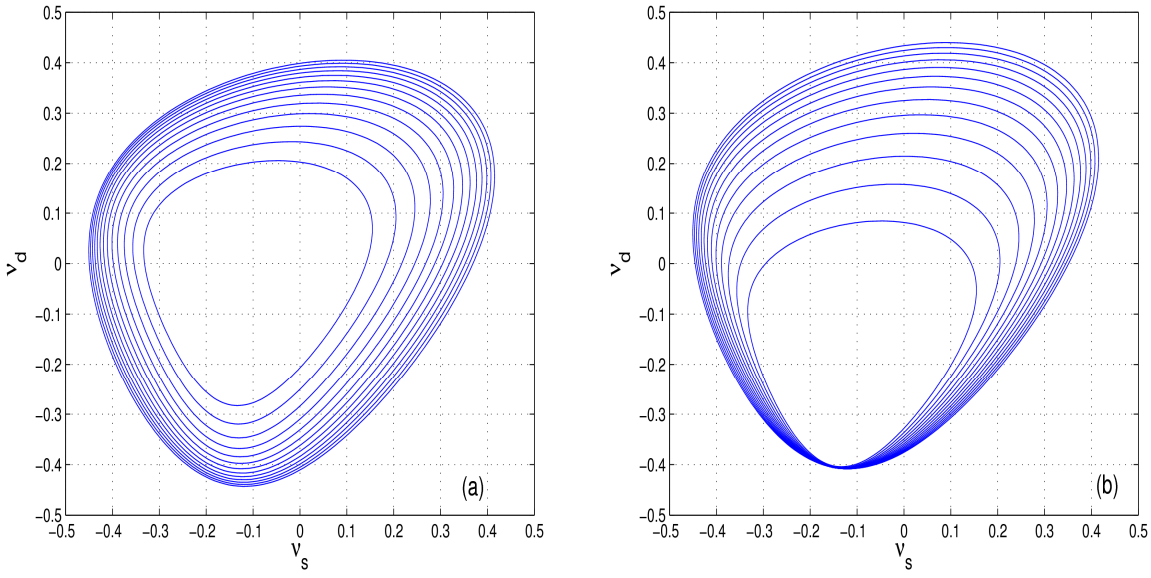

Figure 3. (a) DD curves before Doppler warping. (b) DD curves after Doppler warping.

The main advantage of DW is its simplicity of implementation. However, DW requires that the shape of the DD curves or, equivalently, the configuration be known. Furthermore, DW provides range-dependence compensation only at a single (ν_s,ν_d) point. The compensation for other (ν_s,ν_d) points is only acceptable if the DD curves do not vary too much with range. This is, for example, the case for nearly-sidelooking MS configurations. Performance degrades as one moves away from nearly-sidelooking MS configurations and is quite poor for BS configurations.

4.2 Angle-Doppler compensation (ADC)

One of the drawbacks of DW is that this method aligns the clutter ridges in the Doppler dimension only. DW does not take into account the influence of the amplitude of the antenna pattern at each (ν_s,ν_d) point along each DD curve. For highly-directive transmit antennas, however, the clutter energy is mainly concentrated around one (ν_s,ν_d) point on each DD curve. This point is referred to as the spectral center for the curve. The concept of spectral center was first introduced in [20]. The idea of ADC is to register the spectral centers at range k with the spectral center at the reference range l [20]. This can be achieved by a 2D translation in the spectral domain (as opposed to 1D "vertical" for DW). This is illustrated in Fig. 4, where Figs. 4a and 4b show the DD curves at the different ranges before and after registration, respectively.

The angle-Doppler warped snapshot $\underline{\mathbf{y}}_{kl}^{ADC}$ is given by

$$\underline{\mathbf{y}}_{kl}^{ADC} = \underline{\underline{\mathbf{T}}}_{kl}^{ADC}\underline{\mathbf{y}}_{k},$$

where the transformation matrix $\underline{\underline{\mathbf{T}}}_{kl}^{ADC}$ implementing the angle-Doppler warping is given by

$$\underline{\underline{\mathbf{T}}}_{kl}^{ADC} = \mathrm{diag}(1\; e^{j2\pi(\nu_d^{SC}(l)-\nu_d^{SC}(k))}\ldots e^{j2\pi(\nu_d^{SC}(l)-\nu_d^{SC}(k))(M-1)})\otimes$$

$$\mathrm{diag}(1\; e^{j2\pi(\nu_s^{SC}(l)-\nu_s^{SC}(k))}\ldots e^{j2\pi(\nu_s^{SC}(l)-\nu_s^{SC}(k))(N-1)}), \quad (8)$$

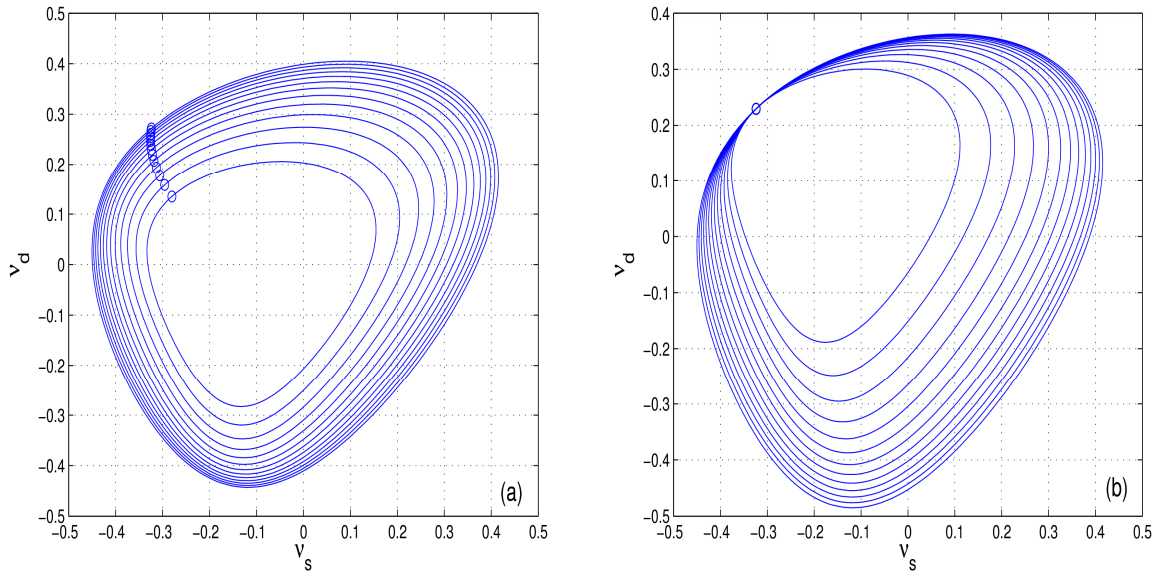

Figure 4. (a) DD curves before angle-Doppler warping. (b) DD curves after angle-Doppler warping.

where $(\nu_s^{SC}(k),\nu_d^{SC}(k))$ and $(\nu_s^{SC}(l),\nu_d^{SC}(l))$ are the (ν_s,ν_d) coordinates of the spectral centers at k and l, respectively. The SMI [14] algorithm can then be applied to the registered snapshots $\underline{\mathbf{y}}_{kl}^{ADC}$.

The main advantage of ADC is also its simplicity of implementation. However, ADC also requires the shape of the DD curves to be known. Furthermore, the registration is valid only for a single (ν_s, ν_d) point, namely the spectral center. ADC is thus valid only for highly-directive transmit antennas.

4.3 Adaptive angle-Doppler compensation (A^2DC)

A^2DC [7] is an enhancement of ADC, whereby the positions of the spectral centers are adaptively estimated from the data.

In A^2DC, one first computes an estimate of the PS of all the snapshots by using, for example, the high-resolution MUSIC algorithm [21]. The maximum value from each PS estimate gives the position of the spectral center. To reduce the computational load, the PS estimate is computed on a reduced-dimension snapshot.

Then, one computes the transformation matrix $\underline{\underline{\mathbf{T}}}_{kl}^{A^2DC}$ to be applied to the secondary-data snapshots as a function of the estimated position of the spectral center. $\underline{\underline{\mathbf{T}}}_{kl}^{A^2DC}$ is given by

$$\underline{\underline{\mathbf{T}}}_{kl}^{A^2DC} = \mathrm{diag}(1\, e^{j2\pi(\hat{\nu}_d^{SC}(l)-\hat{\nu}_d^{SC}(k))} \ldots e^{j2\pi(\hat{\nu}_d^{SC}(l)-\hat{\nu}_d^{SC}(k))(M-1)}) \otimes$$
$$\mathrm{diag}(1\, e^{j2\pi(\hat{\nu}_s^{SC}(l)-\hat{\nu}_s^{SC}(k))} \ldots e^{j2\pi(\hat{\nu}_s^{SC}(l)-\hat{\nu}_s^{SC}(k))(N-1)}),$$

which is the same as the expression in Eq. (8), with the difference that the coordinates of the spectral centers at k and l have been replaced by their estimates $(\hat{\nu}_s^{SC}(k), \hat{\nu}_d^{SC}(k))$ and $(\hat{\nu}_s^{SC}(l), \hat{\nu}_d^{SC}(l))$ at k and l, respectively.

The main advantage of A^2DC over both DW and ADC is that A^2DC does not require the shape of the DD curves to be known. This comes at the price of an additional step, which is the spectral analysis of all the snapshots. Like DW and ADC, A^2DC also suffers from the fact that the registration is performed only for a single (ν_s, ν_d) point. A^2DC is thus also only valid for highly-directive transmit antennas.

4.4 Derivative-based updating (DBU)

DBU uses a time-varying weight vector to accommodate the clutter non-stationarity. It was initially applied to MS configurations using a circular array [22]. It was then applied to BS configurations [6,9]. This method does not perform RDC based on geometrical transformations of DD curves. In this method, the optimum weight vector $\underline{\mathbf{w}}_{o,l'}$ at range k is computed using the Taylor series expansion [23]

$$\underline{\mathbf{w}}_{o,l'} = \underline{\mathbf{w}}_{o,l} + (l'-l)\dot{\underline{\mathbf{w}}}_{o,l} + \cdots,$$

where $\dot{\underline{\mathbf{w}}}$ represents the derivative, with respect to range, of $\underline{\mathbf{w}}$, regarded as a function of range. This expansion is typically limited to first-order derivatives. It could, however, easily be generalized to include high-order derivatives. The values of the augmented weight vector $\tilde{\underline{\mathbf{w}}}_{o,l}$, formed by $\underline{\mathbf{w}}_{o,l}$ and $\dot{\underline{\mathbf{w}}}_{o,l}$, is given by

$$\underline{\tilde{\mathbf{w}}}_{o,l} = \begin{pmatrix} \underline{\mathbf{w}}_{o,l} \\ \underline{\dot{\mathbf{w}}}_{o,l} \end{pmatrix} = \underline{\underline{\mathbf{R}}}^{-1} \begin{pmatrix} \underline{\mathbf{v}}(\nu_s, \nu_d) \\ \underline{0} \end{pmatrix},$$

with

$$\underline{\underline{\mathbf{R}}} = \frac{1}{N_l} \sum_{k \in S_l} \begin{pmatrix} \underline{\underline{\mathbf{R}}}_k & (k-l)\underline{\underline{\mathbf{R}}}_k \\ (k-l)\underline{\underline{\mathbf{R}}}_k & (k-l)^2 \underline{\underline{\mathbf{R}}}_k \end{pmatrix},$$

where $\underline{\underline{\mathbf{R}}}_k = \underline{\mathbf{y}}_k \underline{\mathbf{y}}_k^{\dagger}$. This augmented weight $\underline{\tilde{\mathbf{w}}}_{o,l}$ is then applied to the augmented data vector

$$\underline{\tilde{\mathbf{y}}}_l = \begin{pmatrix} \underline{\mathbf{y}}_l \\ (l'-l)\underline{\mathbf{y}}_l \end{pmatrix}.$$

The performance of the DBU method in the case of non-stationary interference is discussed in [24] for MS configurations with a circular array and for BS configurations with a ULA. A covariance analysis of the performance of DBU can be found in [25].

The main advantage of DBU is that it does not require the knowledge of the shape of the DD curves. There are, however, some drawbacks. First, the degree of success depends on how well a first-order approximation matches the evolution with range of the secondary-data statistics. Better results can be achieved by using higher-order derivatives. Second, there are twice as many coefficients to be estimated in the augmented weight vector. The size of the covariance matrix to be estimated is thus doubled in each dimension and the number of secondary-data snapshots required is thus quadrupled. The computational cost for inverting the covariance matrix is increased by a factor of eight. Combining the DBU with a sub-optimum method such as joint-domain localized (JDL) processing [26] can partially mitigate the need for more secondary data.

5.0 REGISTRATION-BASED COMPENSATION (RBC) METHOD

The DW, ADC, and A^{2}DC methods have poor performance when used with omnidirectional transmit antennas. The reason is that they register the DD curves only at a single (ν_s, ν_d) point. The DBU method relies on the assumption of a linear variation with range of the optimum weight vector and imposes a substantial increase in computational load and in the need for secondary data.

The problems associated with the methods presented above are taken into account by the RBC method developed at the University of Liège, Liège, Belgium, and the Royal Military Academy, Brussels, Belgium [17,27,10,13,28,19,29,30]. We will describe the registration method as presented in [28], which is an improved version of that in [10].

Since the RD phenomenon is most visible in the spectral domain (via the deformation of the clutter ridge), Lapierre et al. [28,10] suggested to perform the RDC in this domain. The idea is to deform the clutter PS $P_{y,k}(U,V)$ at each range $k \in S_l$ to bring its clutter ridge into registration with that of the PS at the range l of interest. We tend to associate (ν_s, ν_d) with a specific scatterer, e.g. on an isorange, and we tend to use (U,V) to denote the coordinates of the spatial and Doppler frequencies. Because of the direct relationship between clutter ridges and DD curves, the algorithm can also be described in terms of DD curves. The advantage of the RBC over DW, ADC, and A^{2}DC is that it is designed to bring the DD curves

into registration, not only at an isolated (ν_s,ν_d) point, but at all the (ν_s,ν_d) points lying on the DD curve. A first version of the RBC method was presented in [10]. An improved version is given in [28]. We begin with a description of the basic principle of the RBC method.

If we assume the configuration parameters known, the clutter covariance matrix can be computed provided the signal power $\sigma_c(\underline{r}(\psi_i))$ scattered by clutter patches along the isorange is known. Hence, the intrinsic goal of the method is to estimate $\sigma_c(\underline{r}(\psi_i))$ along the isorange at the range l of interest. A single-realization estimate of $\sigma_c(\underline{r}(\psi_i))$ at any range $k \in S_l$ can be obtained by estimating the PS at the spatial-Doppler frequencies that correspond to the clutter patch $\underline{r}(\psi_i)$ at range k. The variance of this estimation can then be reduced by averaging single-realization estimates obtained at all ranges $k \in S_l$ at constant ψ_i. In doing so, we assume that the $\sigma_c(\underline{r}(\psi_i))$ at all ranges $k \in S_l$ are iid along lines of constant ψ_i. Measurements at different ranges can safely be considered independent as long as the range resolution is higher than the distance between two successive isoranges. However, the $\sigma_c(\underline{r}(\psi_i))$ will only be identically distributed if the terms of the radar equation are identical and, in particular, if we assume an homogeneous ground cover over the training area and we neglect the variation of the range and the antenna gain over the training area.

As indicated above, a valid PS estimate $P^a_{y,l}(U,V)$ at the range l of interest is found by averaging the properly transformed PS $P_{y,k}(U,V)$ for all $k \in S_l$, i.e.

$$P^a_{y,l}(U,V) = \frac{1}{N_l}\sum_{k\in S_l} T^P_{kl}\left[P_{y,k}(U,V)\right], \quad (9)$$

where $P_{y,k}(U,V)$ is obtained from $\underline{\mathbf{y}}_k$ by a spectral estimation method and $T^P_{kl}[\cdot]$ is the transformation that brings the DD curve at k into registration with that at l. Lapierre et al. do not give an analytical expression for $T^P_{kl}[\cdot]$, but rather an algorithmic description [10,28]. To obtain an estimate $\hat{\underline{\underline{\mathbf{R}}}}^a_l$ of the I+N covariance matrix $\underline{\underline{\mathbf{R}}}_l$ in the space-time domain once $P^a_{y,l}(U,V)$ has been computed, Lapierre et al. propose to compute $\hat{\underline{\underline{\mathbf{R}}}}^a_l$ by applying an "inverse PSD" operation, denoted by the operator $\mathrm{PSD}^{-1}\{\cdot\}$, to $P^a_{y,l}(U,V)$ of Eq. (9), i.e.

$$\hat{\underline{\underline{\mathbf{R}}}}^a_l = \mathrm{PSD}^{-1}\{P^a_{y,l}(U,V)\}.$$

The derivation of a $\mathrm{PSD}^{-1}\{\cdot\}$ operator can be found in [13]. Its expression is given later in Eq. (12).

We continue with a description of the improved version of the RBC method described in [28]. Figure 6 shows the block diagram representing the RBC method. A detailed description of each of its elements follows.

Tuned periodogram

This step consists in estimating the signal power scattered by the clutter patches along the isorange. Assuming $\underline{\theta}$ known, we can compute the DD curve at each range. Thus, the locus of the clutter energy in

the PS estimate is known prior to computing this PS estimate. Instead of computing the periodogram on a rectangular grid in the (U,V)-plane as suggested in [10], it is more efficient to compute the periodogram for a number, say J_C, of (U_C,V_C) points located exactly on the DD curve C of interest [28]. Thus, for a given frequency pair (U_C,V_C), the value of the periodogram is given by

$$P_{y,k}(U_C,V_C)=\frac{1}{NM}\left|\sum_{n=0}^{N-1}\sum_{m=0}^{M-1}y_k(n,m)e^{-j2\pi(nU_C+mV_C)}\right|^2, \qquad (10)$$

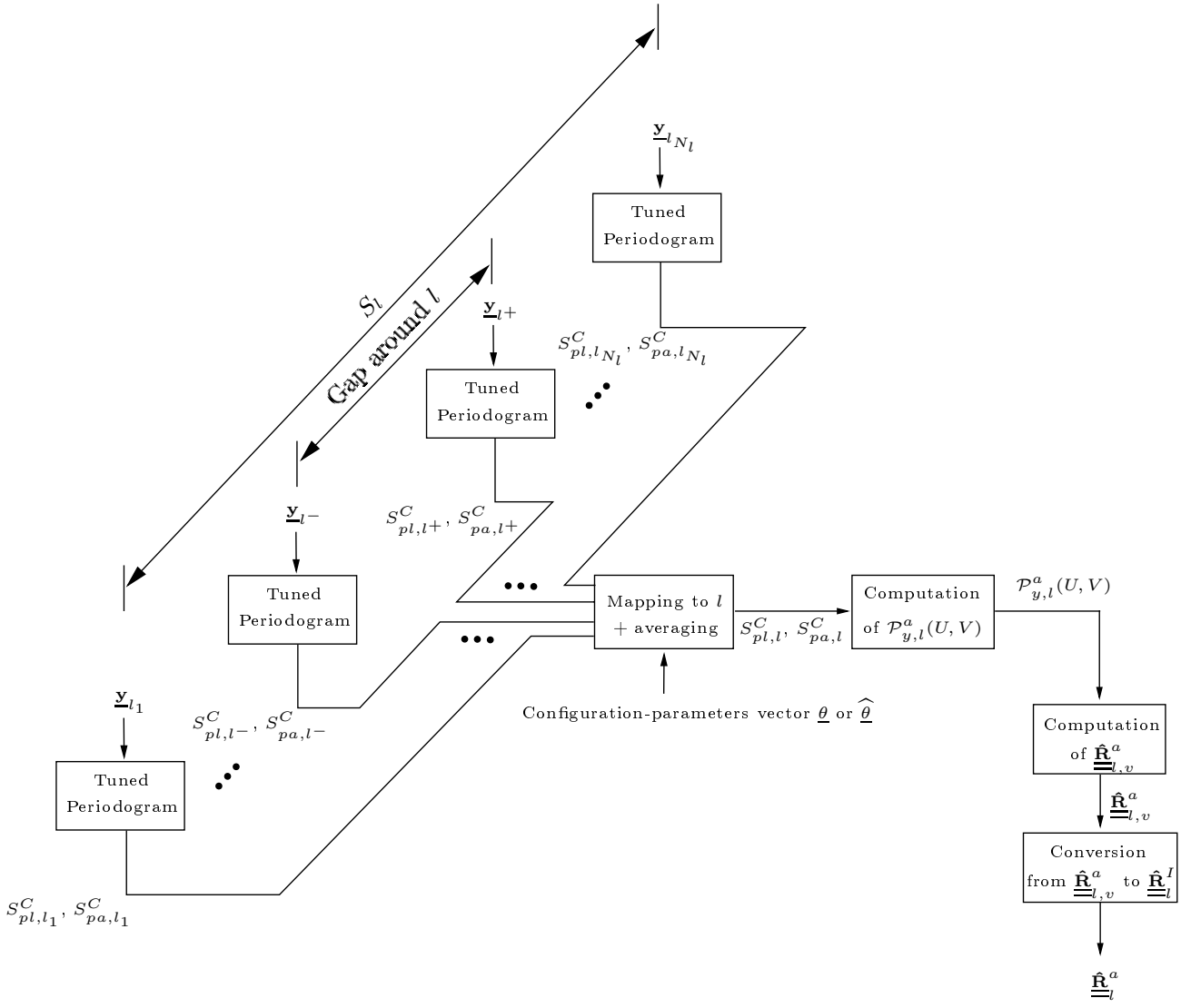

Figure 6. Generic block diagram of the RBC method of [28]. Range indices l_1 and l_{N_l} are the indices of the range gates in S_l with the smallest and the largest ranges, respectively. l^- and l^+ correspond to the indices in S_l just below and just above the guard cells (i.e. the range cells which are not used in the estimation to avoid that clutter estimation be corrupted by targets), respectively.

where $y_k(n,m)$ is the element of $\underline{\mathbf{y}}_k$ that corresponds to the nth antenna element and the mth pulse. The periodogram computed is thus tuned to each (U,V) point located on C, hence the term "tuned periodogram" used in [28]. Ideally, the tuned periodogram of Eq. (10) must be computed for all points lying on C. In practice, Eq. (10) is computed only for a discrete set $S_{pl,k}^C$ of J_C frequency pairs (U_C,V_C) at each range $k \in S_l$.

This set $S_{pl,k}^C$ is obtained by means of the parametric equations $v_s(\psi)=g_1(\psi)$ and $v_d(\psi)=g_2(\psi)$ mentionned in Section 3. The angle ψ is discretized into J_C angles $\psi_j=\psi_0+j\Delta\psi,\ j=0,1,...,J_C-1$, where $\Delta\psi=2\pi/J_C$. The jth $(U_{C,j},V_{C,j})$ frequency pair is given by $(U_{C,j},V_{C,j})=(v_s(\psi_j),v_d(\psi_j))$.

The output of the tuned periodogram at range k consists of the set $S_{pl,k}^C$ and the set $S_{pa,k}^C$ of J_C amplitudes of the J_C extracted peaks with values $P_{y,k}(U_{C,j}(k),V_{C,j}(k))$, corresponding to the locations $(U_{C,j}(k),V_{C,j}(k))$ in $S_{pl,k}^C$, i.e.

$$S_{pa,k}^C=\{P_{y,k}(U_{C,0}(k),V_{C,0}(k)),...,P_{y,k}(U_{C,J_C-1}(k),V_{C,J_C-1}(k))\}.$$

In short, the tuned periodogram at range k takes as input the snapshot $\underline{\mathbf{y}}_k$ and produces the set $S_{pl,k}^C$ of frequency pairs and the set $S_{pa,k}^C$ of amplitudes as output.

Mapping to l + averaging

The input to this stage are the N_l pairs of sets $S_{pl,k}^C$ and $S_{pa,k}^C$ and the configuration parameter vector $\underline{\theta}$. The output is the pair of sets $S_{pl,l}^C$ and $S_{pa,l}^C$ that respectively contain the (U,V) locations of the DD curve at range l and the amplitudes of the PS estimate on this DD curve.

The authors of [28] propose the following method to obtain $S_{pl,l}^C$ and $S_{pa,l}^C$. They consider the jth point $(U_{C,j}(k),V_{C,j}(k))$ in $S_{pl,k}^C$ for each $k \in S_l$. The curve in the (U,V,R_b) space linking the $(U_{C,j}(k),V_{C,j}(k))$, for successive values of k, at a fixed j, is called a "flow line". All N_l points corresponding to the same value of ψ, for example ψ_j, are thus located on the same flow line. The jth value in the set $S_{pl,l}^C$ (at l), denoted by $(U_{C,j}(l),V_{C,j}(l))$, is thus also on the flow line corresponding to ψ_j, but is located at l instead of at k. The jth element of $S_{pa,l}^C$ is denoted by $P_{y,l}(U_{C,j}(l),V_{C,j}(l))$ and is obtained by averaging the jth element in the sets $S_{pa,k}^C$ for all $k \in S_l$, i.e.

$$P_{y,l}(U_{C,j}(l),V_{C,j}(l))=\frac{1}{N_l}\sum_{k\in S_l}P_{y,k}(U_{C,j}(k),V_{C,j}(k)). \quad (11)$$

The output of the "mapping to l + averaging" operation consists of

$$S_{pl,l}^{C} = \{(U_{C,0}(l), V_{C,0}(l)), ..., (U_{C,J_C-1}(l), V_{C,J_C-1}(l))\}$$
$$S_{pa,l}^{C} = \{P_{y,l}(U_{C,0}(l), V_{C,0}(l)), ..., P_{y,l}(U_{C,J_C-1}(l), V_{C,J_C-1}(l))\}.$$

Computation of $P_{y,l}^{a}(U,V)$

The inputs to this element are $S_{pl,l}^{C}$ and $S_{pa,l}^{C}$. The output is $P_{y,l}^{a}(U,V)$. $P_{y,l}^{a}(U,V)$ is considered to be zero except for the (U,V) points that are in $S_{pl,l}^{C}$. The value of $P_{y,l}^{a}(U,V)$ at a point in $S_{pl,l}^{C}$ is equal to the corresponding value in the set $S_{pa,l}^{C}$.

Computation of $\hat{\underline{\underline{\mathbf{R}}}}_{l,v}^{a}$

In this step, the authors of [28] compute an estimate of the representation of the covariance matrix in the (U,V)-plane. This estimate, denoted by $\hat{\underline{\underline{\mathbf{R}}}}_{l,v}^{a}$, is obtained by

$$(\hat{\underline{\underline{\mathbf{R}}}}_{l,v}^{a})_{V_pN+U_q, V_rN+U_s} = \gamma \sum_{j=1}^{J_C-1} \frac{1}{\Delta C_j} P_{y,l}^{a}(U_{C,j}(l), V_{C,j}(l))$$
$$\left(\frac{\sin(\pi M(\frac{V_p}{M} - V_{C,j}(l)))}{\sin(\pi(\frac{V_p}{M} - V_{C,j}(l)))}\right)\left(\frac{\sin(\pi N(\frac{U_q}{N} - U_{C,j}(l)))}{\sin(\pi(\frac{U_q}{N} - U_{C,j}(l)))}\right)$$
$$\left(\frac{\sin(\pi M(\frac{V_r}{M} - V_{C,j}(l)))}{\sin(\pi(\frac{V_r}{M} - V_{C,j}(l)))}\right)\left(\frac{\sin(\pi N(\frac{U_s}{M} - U_{C,j}(l)))}{\sin(\pi(\frac{U_s}{N} - U_{C,j}(l)))}\right), \quad (12)$$

where $\gamma = e^{-j\pi[\frac{N-1}{N}(U_q - U_s) + \frac{M-1}{M}(V_r - V_p)]}/NM$ and ΔC_j is the distance, along C, between the point $(U_{C,j-1}(l), V_{C,j-1}(l))$ and the point $(U_{C,j}(l), V_{C,j}(l))$. The proof for this expression can be found in [13].

Conversion from $\hat{\underline{\underline{\mathbf{R}}}}_{l,v}^{a}$ to $\hat{\underline{\underline{\mathbf{R}}}}_{l}^{a}$

The final step is to convert the space-time frequency domain $\hat{\underline{\underline{\mathbf{R}}}}_{l,v}^{a}$ to its space-time domain representation $\hat{\underline{\underline{\mathbf{R}}}}_{l}^{a}$ by using

$$\hat{\underline{\underline{\mathbf{R}}}}_{l}^{a} = \underline{\underline{\mathbf{V}}}^{\dagger} \hat{\underline{\underline{\mathbf{R}}}}_{l,v}^{a} \underline{\underline{\mathbf{V}}},$$

where $\underline{\underline{\mathbf{V}}}$ contains the coefficients of the 2D DFT [28]. The matrix $\hat{\underline{\underline{\mathbf{R}}}}_l^a$ constitutes the estimate of the clutter covariance matrix.

These last two steps are strictly equivalent to a synthesis of the covariance matrix from the estimated scattered signal power $P_{y,l}(U_{C,j}(l),V_{C,j}(l))$. It should again be stressed that, strictly speaking, this is only possible if we assume a known geometric configuration. In practice, we may need to estimate this configuration.

The advantage of the RBC method used in conjunction with the configuration parameter estimation method is that it can be used for any BS configuration. Indeed, the shape of the DD curves for every BS configuration can be estimated from the data and the registration phase of the algorithm achieves registration for all the points on the DD curves.

6.0 Configuration parameter estimation

Most RD compensation methods described above assume that the shape of the DD curves are known, or equivalently, that the geometric configuration parameters are known. A method to estimate the configuration parameters was presented in [10] and refined in [19]. Another, very similar method is described in [34]. We will now detail the first two methods. The main motivation for these estimation methods is that the clutter energy of a snapshot at a given range is mostly concentrated along the corresponding DD curve and that this DD curve only depends on the configuration parameters. Indeed, by definition, the scatterers contributing to clutter energy are located on the isorange corresponding to each BS range of interest. To each scatterer at a specific position along this isorange corresponds a specific pair of spatial and Doppler frequencies and, hence, a specific point on the DD curve. The idea underlying this estimation method is to fit a mathematical model of the DD surface to the energy extracted at all the ranges of interest comprised in the data cube. This can be seen as fitting a theoretical model of the DD surface to a measured DD surface. The configuration parameter estimation method consists in two steps: (1) peak extraction, and (2) DD-surface fitting.

6.1 Peak extraction

The peak-extraction step is to be applied to every snapshot in the coherent processing interval, but it is described here for the particular snapshot $\underline{\mathbf{y}}_k$. First, a PS estimate is obtained by computing the periodogram of $\underline{\mathbf{y}}_k$. Zero-padding is applied to the snapshot to obtain a smooth 2D PS estimate. Only the largest local maxima are kept, thus discarding spurious peaks due to noise and other artifacts.

An illustration of the outcome of this step is the peak constellation shown in Fig. 5. Ideally, these peaks should fall on the underlying DD surface. In practice, they will generally fall close to it. This constellation of peaks is the input to the subsequent DD-surface fitting step.

6.2 DD-surface fitting

The DD-surface fitting step starts from the 3D constellation of points (extracted-peak locations), which can be thought of as lying on an experimental, i.e. measured, DD surface that hopefully approximates well the underlying theoretical DD surface. Our goal is to recover the vector $\underline{\theta}$ that characterizes the underlying theoretical DD surface.

The DD-surface fitting step requires the definition of a cost function that is related to the distance between the measured DD surface and the theoretical DD surface. The chosen cost function is defined as the RMS euclidean distance between the locations of the peaks and the theoretical DD surface. To reduce the complexity of the method, this cost function is approximated by computing the required distances only in horizontal planes, i.e. at constant ranges [19]. Two strategies are used in succession to eliminate or mitigate the influence of potentially-spurious peaks that could not be eliminated by thresholding in the peak-extraction step. First, peaks located at distances larger than five times the mean distance are discarded. Second, the contribution of each peak to the cost function is weighted by the amplitude of the peak. Indeed, low-amplitude peaks are more likely to be spurious, while large-amplitude peaks are more likely to be due to a return form a ground-clutter patch [19].

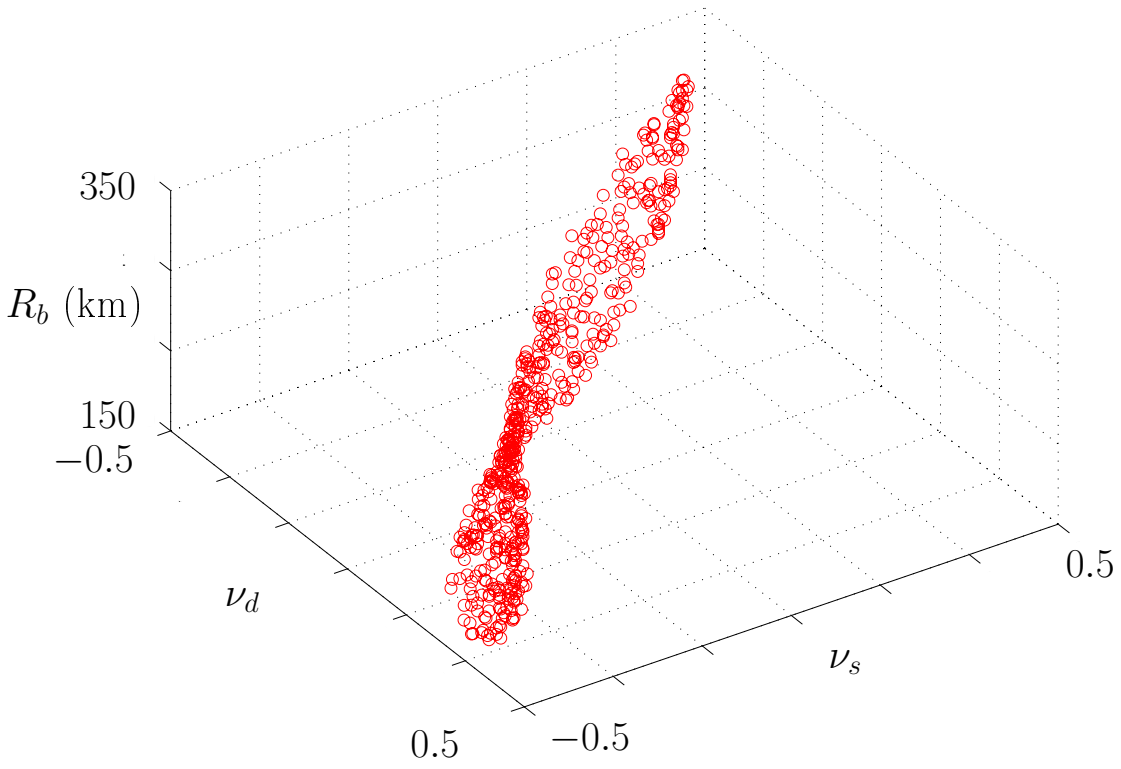

Figure 5. 3D scatter plot of extracted peak locations in (ν_s, ν_d, R_b) -axes. The peaks are located in the horizontal slices corresponding to the ranges present in the data cube. The complete collection of peaks is the input to the DD-surface fitting step.

To minimize the cost function, one can, for example, use a variation of the simplex algorithm as suggested in [19]. This algorithm has the advantage that no analytic expression of the derivative of the cost function with respect to the parameters is needed. It is clear that a strategy must be developped to avoid spurious local-minima solutions and to reach the global minimum. The strategy proposed by [19] consists in splitting the estimation of the parameter vector in several stages. At each stage, only a subset of the parameters is estimated. Reference [19] proposes three distinct submethods, each one providing its own individual estimate of the parameter vector as well as the corresponding value of the cost function. The order in which the parameter subsets are estimated and the initial values are used differentiate these three submethods. Each submethod is guided by a different aspect of the physical insight about the problem. The overall estimation is obtained by picking the estimate associated with the lowest cost. The description of the three submethods is beyond the scope of this paper. The reader should consult [19] for details.

The output of the DD-surface fitting step is the estimate $\hat{\underline{\theta}}$ of $\underline{\theta}$.

7.0 4D DIRECTION-DOPPLER (DD) CURVES

The RBC method presented in Section 5 is based on the concept of DD curves. In [10,13,28], the RBC method is restricted to ULAs. It is, however, possible to extend the RBC method to arbitrary antenna arrays such as CAAs, provided an appropriate spectral description of the recorded data and an accurate description of the clutter PS locus is used. Therefore, in Section 7.1, we first introduce a spectral representation for arbitrary antenna arrays, which contain CAAs as a special case, and explain its link to that used for ULAs. Then, in Section 7.2, we discuss the RD problem in this more general case. Finally, in Section 8, we present the extended version of the registration phase of the RBC method. A configuration parameter estimation phase for CAAs is currently being implemented.

7.1 Spectral representation for arbitrary antenna arrays

An introduction to the spectral representation for space-time signals recorded by an arbitrary antenna arrays, and thus by CAAs, is given in [11]. In this section, we recall the elements of this representation that are vital to the understanding of the extension of the registration phase to CAAs. The clutter patches contributing to the ground clutter in a snapshot at a given range are located on the corresponding isorange. The signal reflected by each clutter patch along this isorange is characterized by a particular pair $(\underline{\mathbf{k}},\omega)$, where $\underline{\mathbf{k}}$ is the wavevector and ω the Doppler pulsation. Hence, the signal from each clutter patch corresponds to a distinct point in the 4D clutter PS or, equivalently, to a particular point in the 4D space-time "frequency" domain $(\underline{\mathbf{k}},\omega)$ representing the incoming signal [11]. Each snapshot is the result of the contribution of all the clutter patches along the corresponding isorange. Hence, the support of the clutter PS in the 4D space-time frequency domain $(\underline{\mathbf{k}},\omega)$ is represented by a continuous curve. For a range R_b, this 4D curve is called, in [11], the 4D clutter PS locus. In this paper, we call this 4D clutter PS locus a 4D DD curve. For a given wavelength λ and pulse repetition interval PRI, this curve depends only on the configuration parameters, lumped in $\underline{\theta}$, and the range R_b under consideration. Figure 7 shows an illustration of a 4D DD curve. The coordinate systems in the graphs are normalized as follows. The normalized spatial frequency vector $\underline{\nu}_s = (\nu_{sa}, \nu_{sc}, \nu_{sv})$ and the wavevector $\underline{\mathbf{k}} = (k_x, k_y, k_z)$ are linked by $\underline{\nu}_s = \underline{\mathbf{k}}\lambda/(2\pi)(1/2)$. The relation between the normalized Doppler frequency ν_d and the Doppler pulsation ω is $\nu_d = \omega\mathrm{PRI}/(2\pi)$. Figure 7 is made up of two graphs. The first graph is the projection of the 4D DD curve in the 3D space (k_x, k_y, ω), while the second graph is its projection in the 3D space (k_x, k_y, k_z). For a given wavelength λ, the norm of $\underline{\mathbf{k}}$ is constant and, thus, the second projection of the 4D DD curve is located on a sphere. It is important to note that, for a given wavelength and a given PRI, each 4D DD curve depends only on $\underline{\theta}$, and, in particular, not on the shape of the antenna array used at the receiver. The concept of 4D DD curves is thus valid for arbitrary 3D receiver arrays, which include the particular cases of ULAs, planar arrays, and CAAs.

In practice, one cannot observe the 4D DD curves directly. One can only obtain estimates thereof. This is due to (a) the finite extent of the radar antenna and the finite length of the train of pulses, and (b) the random nature of the clutter snapshots. It can be shown that the clutter PS and its estimate are linked by a convolution operation, which implies that, in the clutter PS estimate, the energy due to clutter is still centered on the 4D DD curve [11,31]. This is illustrated in Fig. 8 for a spherical antenna with $N = 76$ elements.

Let us examine more carefully the reason for the 4D-frequency representation introduced above for the clutter PS corresponding to an arbitrary antenna array. Let us consider a possibly complex-valued, continuous, space-time random process $y(\underline{\mathbf{r}},t)$ with zero mean. The four independent variables are the

three spatial coordinates (x, y, z) corresponding to $\underline{\mathbf{r}}$ and the time t. The random process $y(\underline{\mathbf{r}}, t)$ is further assumed to be wide-sense stationary in space and time. Hence, its statistical correlation (covariance) function can be written as

$$r_y(\Delta\underline{\mathbf{r}}, \Delta t) = E\{y(\underline{\mathbf{r}}, t)y^*(\underline{\mathbf{r}} - \Delta\underline{\mathbf{r}}, t - \Delta t)\}.$$

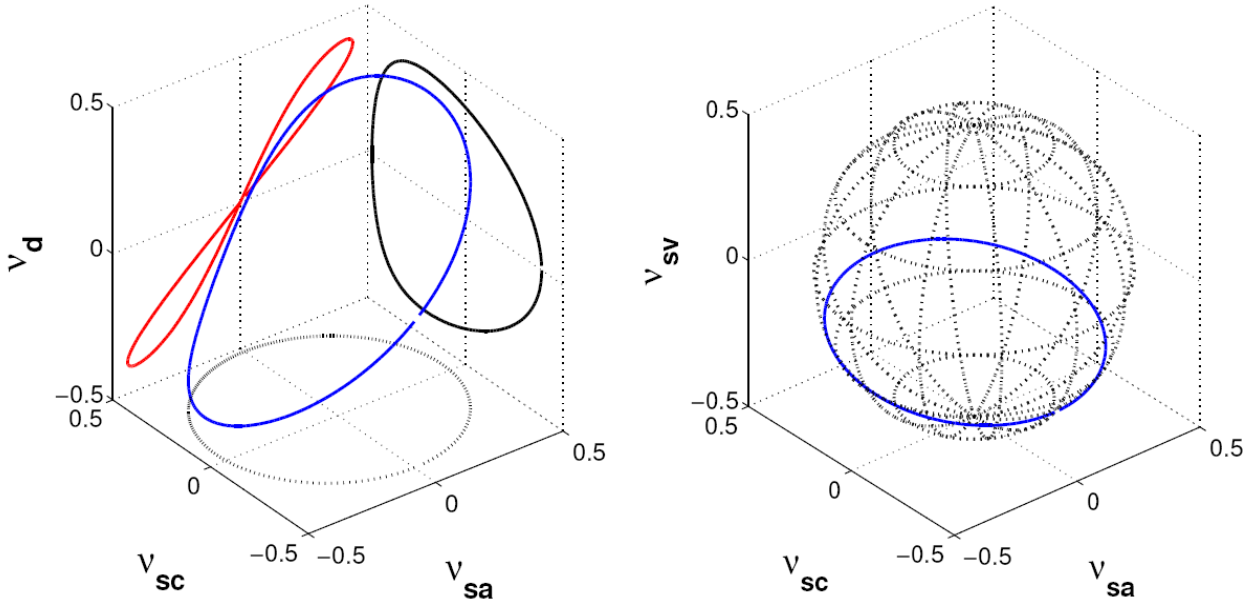

Figure 7. 4D DD curve for a BS wing-to-wing configuration and for a given range R_b. The blue line shows the projected 4D DD curve for that range. The red, black, and dotted-black lines show projections of the 4D DD curve on the (ν_{sa}, ν_d)-plane, the (ν_{sc}, ν_d)-plane, and the (ν_{sa}, ν_{sc})-plane, respectively.

The 4D PS of the random process $y(\underline{\mathbf{r}}, t)$ is the Fourier transform $P_y(\underline{\mathbf{U}}, V)$ of its covariance function [32,31],

$$P_y(\underline{\mathbf{U}}, V) = \iiint \int_{-\infty}^{\infty} r_y(\Delta\underline{\mathbf{r}}, \Delta t) e^{-j2\pi(\underline{\mathbf{U}}\cdot\Delta\underline{\mathbf{r}} + Vt)} d\Delta\underline{\mathbf{r}} d\Delta t,$$

where $(\underline{\mathbf{U}}, V) = (U_{sa}, U_{sc}, U_{sv}, V)$ are the frequency variables, which is a notation that is consistent with the notation (U, V) used in the ULA case.

For a ULA aligned with the x-axis, the correlation function $r_y(\Delta\underline{\mathbf{r}}, \Delta t) = r_y(\Delta x, \Delta y, \Delta z, \Delta t)$ can only be measured for lags of the $(\Delta x, 0, 0, \Delta t)$-type. In other words, we can only "measure" $r_y(\Delta x, 0, 0, \Delta t)$, which we can then treat as the 2D function $r_y = (\Delta x, \Delta t)$. The 2D Fourier transform $P_y(U, V)$ of this function is the 2D PS used in the context of ULAs. The link between the 2D function $P_y(U, V)$ and the

4D function $P_y(\underline{\mathbf{U}},V)$ is given by the projection-slice theorem of computed tomography [33] (with domains reversed). The generalized theorem tells us that

$$P_y(U,V)=\int\int_{-\infty}^{\infty} P_y(U_{sa},U_{sc},U_{sv},V)dU_{sc}dU_{sv}.$$

This relation can easily be proved from first principles. The power of the theorem lies in the fact that it also applies to any orientation of the ULA.

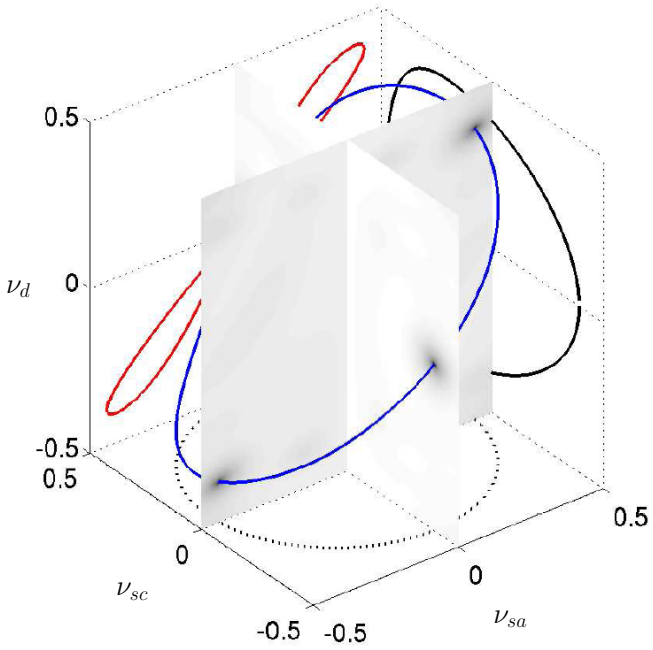

Figure 8. Slices parallel to (ν_{sa},ν_d)-plane and (ν_{sc},ν_d)-plane of the 4D clutter PS estimate (grayscale) with the corresponding 4D DD curve (blue line) for a BS wing-to-wing configuration. The red, black, and dotted-black lines show projections of the 4D DD curve on the (ν_{sa},ν_d)-plane, the (ν_{sc},ν_d)-plane, and the (ν_{sa},ν_{sc})-plane, respectively.

7.2 Range-dependence for CAAs

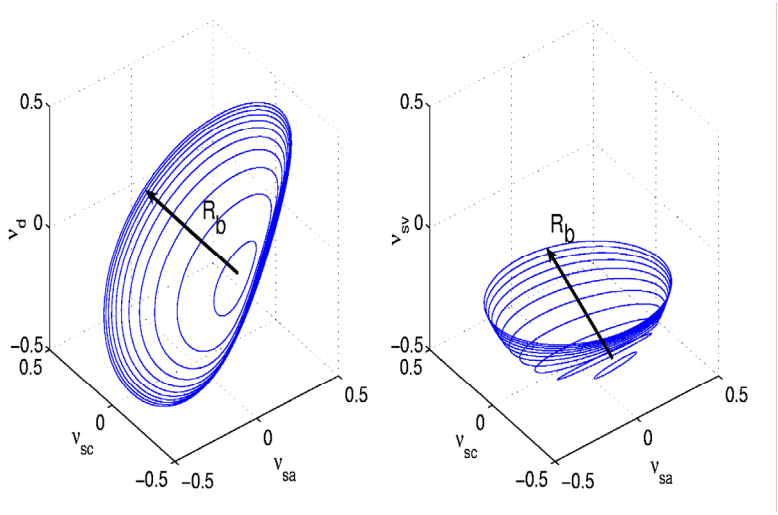

Figure 9. Evolution of the 4D DD curves for increasing range R_b in the case of a BS wing-to-wing configuration.

For most MS and BS configurations, the 4D DD curves depend on the range of interest. Figure 9 illustrates this effect for a BS configuration. The configurations for which there is no range-dependence can be found by physical reasoning about the spatial and Doppler frequencies. One condition to be fulfilled for the 4D DD curve to be independent of range is that the curves at different ranges need to overlap in the 3D space of the spatial frequencies. Since the v_{sc}-coordinate of points along the curves in the 3D space of the spatial frequencies only depends on the elevation angle at which the scatterers along the isoranges are seen from the receiver, overlap in the 3D space of the spatial frequencies occurs if and only if the receiver is on the (flat) ground. In this case, the scatterers are seen at an elevation angle of zero regardless of range. A second condition is that the Doppler frequency must be range-independent. We thus require that the Doppler frequency corresponding to a particular direction of arrival be independent of range. In a configuration where the receiver is located on the ground, the Doppler frequency shift due to the receiver velocity will be constant along radial lines from the receiver. The only configurations for which the Doppler frequency shift induced by the transmitter velocity is independent of range are the following:

1. The transmitter is static, in which case the Doppler frequency is zero and thus range-independent.

2. The transmitter is located on the ground and at the same location as the receiver, in which case the Doppler frequency only depends on the transmitter azimuth angle (and on the transmitter velocity which is range-independent).

Similarly to the case of ULAs, the range-dependence problem in the case of CAAs leads to erroneous covariance matrix estimates and thus to losses in detection performance [11].

The next section generalizes the RBC method discussed in Section 5 for ULAs to the case of CAAs.

8.0 EXTENSION TO CAAS OF THE RBC METHOD

The original method derived for ULAs relies on the registration of the 2D DD curves. The extension of the method to 4D DD curves, thus, essentially consists in adapting the registration of 2D curves to that of 4D curves. For each of the five steps described in Section 5, we describe the modifications required for it to work with 4D DD curves.

Tuned periodogram

Again, the knowledge of $\underline{\theta}$, or of an estimate $\hat{\underline{\theta}}$, allows one to compute the 4D DD curve at each range. Instead of computing a spectral estimate along the corresponding 2D DD curve in the 2D frequency plane (U,V), we compute it along the 4D DD curve in the 4D frequency space $(\underline{\mathbf{U}},V)=(U_{sa},U_{sc},U_{sv},V)$.

The output of the tuned periodogram at range k consists of the pair of sets

$$S_{pl,k}^{C}=\{(\underline{\mathbf{U}}_{C,0}(k),V_{C,0}(k)),\ldots,(\underline{\mathbf{U}}_{C,J_C-1}(k),V_{C,J_C-1}(k))\}$$
$$S_{pa,k}^{C}=\{P_{y,k}(\underline{\mathbf{U}}_{C,0}(k),V_{C,0}(k)),\ldots,P_{y,k}(\underline{\mathbf{U}}_{C,J_C-1}(k),V_{C,J_C-1}(k))\},$$

which contain the J_C locations on the 4D DD curve and the corresponding amplitudes, respectively.

Mapping to l + averaging

To obtain the pair of sets $S_{pl,l}^{C}$ and $S_{pa,l}^{C}$ that contain the frequency pair locations of the 4D DD curve at range l and the corresponding amplitudes of the PS estimate on this 4D DD curve, the averaging operation in Eq. (11) is simply extended to account for a 4D argument, i.e.

$$P_{y,l}(\underline{\mathbf{U}}_{C,j}(l),V_{C,j}(l))=\frac{1}{N_l}\sum_{k\in S_l}P_{y,k}(\underline{\mathbf{U}}_{C,j}(k),V_{C,j}(k)).$$

Computation of $P_{y,l}^{a}(\underline{\mathbf{U}},V)$, Computation of $\hat{\underline{\underline{\mathbf{R}}}}_{l,v}^{a}$, and Conversion from $\hat{\underline{\underline{\mathbf{R}}}}_{l,v}^{a}$ to $\hat{\underline{\underline{\mathbf{R}}}}_{l}^{a}$

In [11], these three operations are called the synthesis step. They produce the space-time covariance matrix estimate from the output of the preceding step. For further information on the synthesis step, the reader should consult [11].

9.0 PRELIMINARY RESULTS

Figure 10 show performance results of the OP, the SMI algorithm, and the RBC method extended to CAAs in terms of $\mathrm{SINR_L}$ for a spherical antenna. We see that the RBC method outperforms the SMI algorithm. Indeed the RBC curve is almost superimposed on the curve of the OP.

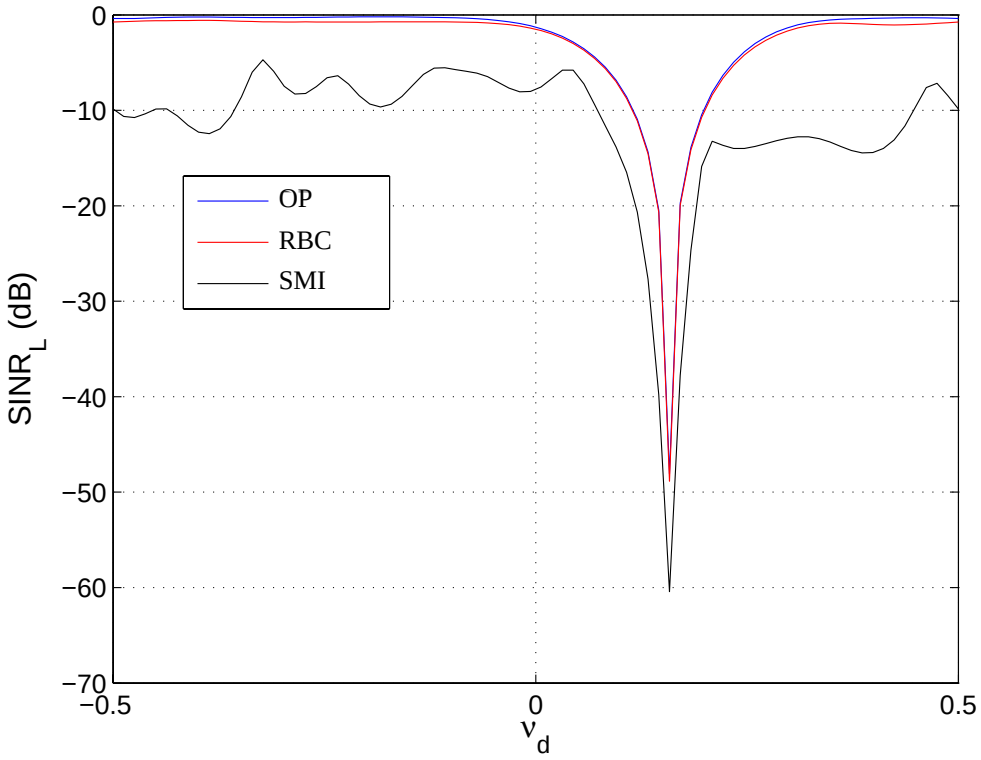

Figure 10. $SINR_L$ curves for the optimum processor (OP), the RBC method extended to CAAs (RBC), and the sample matrix inversion algorithm (SMI) in the case of a spherical antenna array.

10.0 CONCLUSION

In this paper, we examined the range-dependence compensation for STAP for bistatic geometries and arbitrary antenna arrays. We first examined the DW, ADC, A^2DC, and DBU methods, which give acceptable results for restricted operational settings. Limitations concern either the transmit antenna, which must be highly directional (DW, ADC, A^2DC), or the variation of the statistical properties of the secondary data, which must be linear with respect to range (DBU). The RBC method, however, imposes no restriction on the beampattern of the transmit antenna, or on the evolution with range of the statistics of the secondary data. We also showed that an appropriate extension of the RBC method allows one to handle any conformal antenna array and even any arbitrary antenna array at the receiver. We also gave a glimpse of the role of the projection-slice theorem in dealing with PS spectra in the context of STAP, in particular to relate the 2D PS of a ULA to its more general 4D PS.

Acknowledgements

This work was supported by a fellowship of the FNRS (Fonds National de Recherche Scientifique), Brussels, Belgium.

References

[1] G. Stimson. Introduction to Airborne Radar, 2nd Edition. SciTech Publishing Incorporated, May 1999.

[2] R. Klemm. Principles of space-time adaptive processing. IEE Radar, Sonar, Navigation, and Avionics 9, 2002.

[3] R. Boyle and W. Wasylkiwskyj. Comparison of monostatic and bistatic bearing estimation performance for low RCS targets. IEEE Transactions on Aerospace and Electronics Systems (AES), 30(3):962–967, 1994.

[4] A. Prentice. A digitally beamformed phased array receiver for tactical bistatic radar. In IEE Colloquium on Active and Passive Components for Phased Array System, London, UK, 24 April 1992.

[5] G.K. Borsari. Mitigating effects on STAP processing caused by an inclined array. In IEEE National Radar Conference, Dallas, TX, 12-13 May 1998.

[6] W.L. Melvin, M.J. Callahan, and M.C. Wicks. Adaptive clutter cancellation in bistatic radar. In 34th Asilomar Conference on Signals, Systems, and Computer, Pacific Grove, CA, 29 Oct. - 1 Nov. 2000.

[7] W.L. Melvin, B. Himed, and M.E. Davis. Doubly adaptive bistatic clutter filtering. In IEEE National Radar Conference, Hunstville, AL, 5-8 May 2003.

[8] F. Pearson and G. Borsari. Simulation and analysis of adaptive interference suppression for bistatic surveillance radars. In Adaptive Sensor Array Processing Workshop, MIT Lincoln Laboratory, Lexington, MA, 13-14 March 2001.

[9] S.M. Kogon and M.A. Zatman. Bistatic STAP for airborne radar systems. In Adaptive Sensor Array Processing Workshop, MIT Lincoln Laboratory, Lexington, MA, 13-14 March 2000.

[10] F.D. Lapierre and J.G. Verly. Registration-based method for range-dependence compensation in bistatic radar STAP operating on simulated stochastic snapshots. EURASIP JASP Journal, 1:235–245, 2005.

[11] X. Neyt, P. Ries, J.G. Verly, and F.D. Lapierre. Registration-based range-dependence compensation method for conformal array STAP. In Adaptive Sensor Array Processing Workshop, MIT Lincoln Laboratory, Lexington, MA, 7-8 June 2005.

[12] J. Ward. Space-time adaptive processing for airborne radar. Technical Report 1015, MIT Lincoln Laboratory, Lexington, MA, 1994.

[13] F.D. Lapierre. Registration-based Range-dependence Compensation in Airborne Bistatic Radar STAP. PhD thesis, University of Liège, Liège, Belgium, November 2004.

[14] L.E. Brennan and L.S. Reed. Theory of adaptive radar. IEEE Transactions on Aerospace and Electronic Systems (AES), 9(2):237–252, 1973.

[15] N.R. Goodman. Statistical analysis based on a certain multivariate complex gaussian distribution (an introduction). Annals of Mathematical Statistics, 34:152–177, 1963.

[16] I.S. Reed, J.D. Mallett, and L.E. Brennan. Rapid convergence rate in adaptive arrays. IEEE Transactions on Aerospace and Electronic Systems (AES), 10(6):853–863, 1974.

[17] F.D. Lapierre and J.G. Verly. Registration-based solutions to the range-dependence problem in STAP radars. In Adaptive Sensor Array Processing Workshop, MIT Lincoln Laboratory, Lexington, MA, 11-13 March 2003.

[18] R.K. Hersey, W.L. Melvin, and J.H. McClellan. Clutter limited detection performance of multi-channel conformal arrays. Signal Processing, 84:1481–1500, May 2004.

[19] X. Neyt, F.D. Lapierre, and J.G. Verly. Automatic configuration-parameter estimation and range-dependence compensation using simulated, single-realization, random snapshots in STAP. In Adaptive Sensor Array Processing Workshop, MIT Lincoln Laboratory, Lexington, MA, 16-18 March 2004.

[20] B. Himed, Y. Zhang, and A. Hajjari. STAP with angle-Doppler compensation for bistatic airborne radars. In IEEE National Radar Conference, Long Beach, California, 22-25 May 2002.

[21] D.G. Manolakis, V.K. Ingle, and S.M. Kogon. Statistical and Adaptive Signal Processing. McGraw-Hill, 2000.

[22] M. Zatman. Circular array STAP. IEEE Transactions on Aerospace and Electronic Systems (AES), 36(2):510–517, 2000.

[23] S.D. Hayward. Adaptive beamforming for rapidly moving arrays. In IEEE International Radar Conference, Beijing, 8-10 October 1996.

[24] M.A. Zatman. The properties of adaptive algorithms with time varying weights. In Proc. of IEEE Sensor Array Multichannel Signal Processing Workshop, Cambridge, MA, 16-17 March 2000.

[25] M.A. Zatman. Performance analysis of the derivative based updating method. In Adaptive Sensor Array Processing Workshop, MIT Lincoln Laboratory, Lexington, MA, 13-14 March 2001.

[26] H. Wang and L. Cai. On adaptive spatial-temporal processing for airborne surveillance radar systems. IEEE Transactions on Aerospace and Electronic Systems (AES), 30(3):660–669, 1994.

[27] F.D. Lapierre, M. Van Droogenbroeck, and J.G. Verly. New solutions to the problem of range dependence in bistatic STAP radars. In IEEE National Radar Conference, Huntsville, AL, 5-8 May 2003.

[28] F.D. Lapierre and J.G. Verly. Computationally-efficient range-dependence compensation method for bistatic radar STAP. In IEEE National Radar Conference, Arlington, VA, 9-12 May 2005.

[29] X. Neyt, F.D. Lapierre, and J.G. Verly. Estimation of geometric radar configuration parameters for range-dependence compensation in STAP in the presence of targets, jammers, and decorrelation effects. In IEEE Sensor Array and Multichannel Signal Processing (SAM) Conference, Barcelona - Sitges, Spain, 18-21 July 2004.

[30] X. Neyt, F.D. Lapierre, and J.G. Verly. Evaluation of a method for estimating configuration parameters in bistatic radars using directive antennas. In IEEE International Radar Conference 2004, Toulouse, France, 19-21 October 2004.

[31] J. Capon. High resolution frequency wavenumber spectrum analysis. Proceedings of IEEE, 57(8):1408–1418, 1969.

[32] H.L. Van Trees. Detection, estimation, and modulation theory, Part IV: Optimum Array Processing. John Wiley and Sons, 2002.

[33] Robert M. Gray and Joseph W. Goodman. Fourier Transforms: An Introduction for Engineers. Kluwer Academic Publishers, 1995.

[34] Amin G. Jaffer, Braham Himed, and Phuoc T. Ho. Estimation of Range-Dependent Clutter Covariance by Configuration System Parameter Estimation. . In IEEE National Radar Conference, Arlington, VA, 9-12 May 2005.